

ARTICLE

Open Access

# Unveiling the origin of the large coercivity in (Nd, Dy)-Fe-B sintered magnets

Xin Tang<sup>1,2</sup>, Jiangnan Li<sup>1</sup>, Hossein Sepehri-Amin<sup>1,3</sup>, Anton Bolyachkin<sup>1</sup>, Andres Martin-Cid<sup>4</sup>, Shintaro Kobayashi<sup>4</sup>, Yoshinori Kotani<sup>4</sup>, Motohiro Suzuki<sup>4</sup>, Asako Terasawa<sup>5</sup>, Yoshihiro Gohda<sup>6</sup>, Tadakatsu Ohkubo<sup>1</sup>, Tetsuya Nakamura<sup>3,4</sup> and Kazuhiro Hono<sup>1</sup>

## Abstract

Nd-Fe-B-based permanent magnets are widely used for energy conversion applications. However, their usage at elevated temperatures is difficult due to the relatively low coercivity ( $H_c$ ) with respect to the anisotropy field ( $H_A$ ) of the  $\text{Nd}_2\text{Fe}_{14}\text{B}$  compound, which is typically  $0.2H_A$ . In this work, we found that the coercivity of an  $(\text{Nd}_{0.8}\text{Dy}_{0.2})\text{-Fe-B}$  sintered magnet could reach  $0.4H_A$ , which was twice as high as the  $H_c/H_A$  of its Dy-free counterpart. Detailed microstructural characterizations, density functional theory and micromagnetic simulations showed that the large value of coercivity,  $H_c = 0.4H_A$ , originated not only from the enhanced  $H_A$  of the main phase (intrinsic factor) but also from the reduced magnetization of the thin intergranular phase (extrinsic factor). The latter was attributed to the dissolution of 4 at.% Dy in the intergranular phase that anti-ferromagnetically coupled with Fe. The reduction in the magnetization of the intergranular phase resulted in a change in the angular dependence of coercivity from the Kondorsky type for the Dy-free magnet to the Stoner–Wohlfarth-like shape for the Dy-containing magnet, indicating that the typical pinning-controlled coercivity mechanism began to show nucleation features as the magnetization of the intergranular phase was reduced by Dy substitution.

## Introduction

Hard magnetic materials are essential components for energy-efficient and environmentally friendly technologies<sup>1</sup>. In the last four decades, Nd-Fe-B-based sintered magnets have dominated the market share of high-performance permanent magnets owing to their large energy density and relatively abundant constituent elements, such as Fe and Nd<sup>2,3</sup>. However, for major applications, such as automotive traction motors and wind turbines, the coercivity  $H_c$ , which is the ability to resist demagnetization, is of critical importance for operation at elevated temperatures<sup>1,4,5</sup>. Although the coercivity is known to be theoretically limited by the anisotropy field,  $H_A$ , of the  $\text{RE}_2\text{Fe}_{14}\text{B}$  main phase, where RE

is a rare earth element, such as Nd, Pr, and Dy, only ~20% of the  $H_A$  has thus far been exploited for the coercivity of commercially sintered magnets<sup>6–10</sup>.

Here, we introduce the coercivity ratio  $k = H_c/H_A$ ; this is the coercivity normalized by the anisotropy field of the main phase, where  $k$  indicates how much coercivity, which is a structure-sensitive property, is achieved with respect to  $H_A$  in a particular permanent magnet. An ideal Stoner–Wohlfarth particle, which is a defect-free and magnetically isolated nanocrystal with uniaxial magneto-crystalline anisotropy, could show  $k = 1$  along its easy axis. However, permanent magnets must be an assembly of micron- or submicron-sized polycrystals, and the coercivity reaches  $0.35H_A$  for an ideal model in micro-magnetic simulations considering a weakly ferromagnetic intergranular phase (IGP) and the effect of a demagnetizing field<sup>11</sup>. The coercivity ratio could be further reduced by microstructural defects in heterogeneous regions<sup>9–12</sup>. Tremendous efforts have been made to

Correspondence: Xin Tang (TANG.Xin@nims.go.jp) or Hossein Sepehri-Amin (H.SEPEHRIAMIN@nims.go.jp)

<sup>1</sup>National Institute for Materials Science, Tsukuba 305-0047, Japan

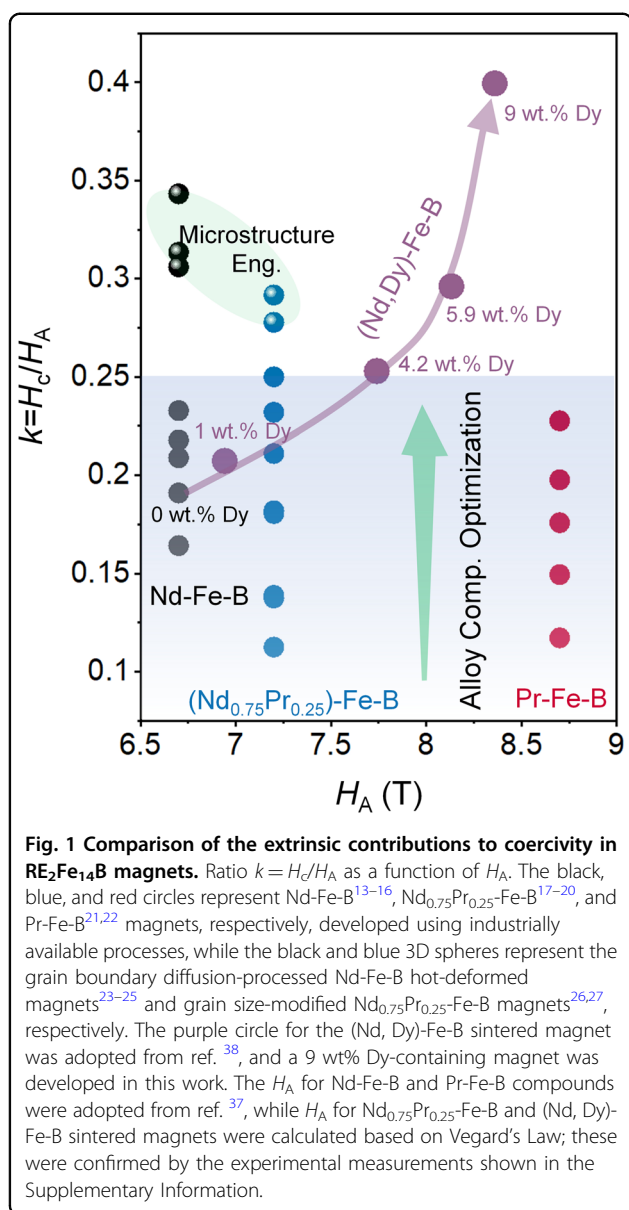
<sup>2</sup>International Center for Young Scientists, National Institute for Materials Science, Tsukuba 305-0047, Japan

Full list of author information is available at the end of the article

© The Author(s) 2023



**Open Access** This article is licensed under a Creative Commons Attribution 4.0 International License, which permits use, sharing, adaptation, distribution and reproduction in any medium or format, as long as you give appropriate credit to the original author(s) and the source, provide a link to the Creative Commons license, and indicate if changes were made. The images or other third party material in this article are included in the article's Creative Commons license, unless indicated otherwise in a credit line to the material. If material is not included in the article's Creative Commons license and your intended use is not permitted by statutory regulation or exceeds the permitted use, you will need to obtain permission directly from the copyright holder. To view a copy of this license, visit <http://creativecommons.org/licenses/by/4.0/>.



maximize  $k$  by optimizing the microstructure. For instance, an increase in the RE content or micro-alloying with trace elements (Al, Cu, Ga) in the alloy composition can improve  $k$  from 0.1 to 0.25, as shown in Fig. 1<sup>13–22</sup>. This result is attributed to the formation of an IGP, which reduces the ferromagnetism of the IGP and strengthens the pinning force against reversed domain propagation<sup>13–22</sup>. Notably,  $k$  is independent of the absolute value of  $H_A$ ; thus, the change in  $k$  for the different types of permanent magnets is caused by an extrinsic origin, such as microstructure optimization, which includes the reduction of magnetism of IGP by a diffusion process<sup>23–25</sup> or the refinement of the grain size<sup>26,27</sup>; these processes are referred to as microstructure engineering in Fig. 1. These efforts have led to a marginal increase in  $k$  up to  $\sim 0.3$ .

Recent micromagnetic approaches have demonstrated a substantial improvement in  $k$  by tuning the hardening mechanism from the pinning-type Kondorsky model to the nucleation-dominated Stoner–Wohlfarth model<sup>28–33</sup>. To date, the magnetic hardening mechanism for RE<sub>2</sub>Fe<sub>14</sub>B magnets (RE = Nd or Pr) is consistent with the pinning-type Kondorsky model, which can be experimentally demonstrated by observing the initial two-step magnetization behavior of submicron grain size magnets<sup>14,34</sup> and by measuring the angular dependence of the coercivity<sup>28–33,35,36</sup>; the initial magnetization curves clearly show an indication of domain wall pinning at IGP and coercivity monotonically increases with the angle between the external field and the easy axis of the magnet. Since the pinning-type mechanism originates from a strong coupling between the hard phase and the soft magnetic intergranular phase<sup>33</sup>, only a small coercivity is obtained for Nd<sub>2</sub>Fe<sub>14</sub>B-based magnets, which limits their applications at elevated temperatures<sup>13–27</sup>. The (Nd, Dy)-Fe-B magnets with a coercivity above 3.0 T are thus far the only option for these applications<sup>5</sup>. The conventional understanding of this high coercivity in (Nd, Dy)-Fe-B sintered magnets is the enhanced anisotropy field by the partial substitution of Nd with Dy in the (Nd<sub>1-x</sub>Dy<sub>x</sub>)<sub>2</sub>Fe<sub>14</sub>B main phase<sup>37,38</sup>. However, as shown in Fig. 1, with increasing Dy substitution for Nd, the  $k$  value also increases, and an exceptionally large  $k$  value of 0.4 is obtained for the 9 wt% Dy-containing (Nd,Dy)-Fe-B sintered magnet. This defies the conventional origin of the large coercivity only from higher  $H_A$ . Explaining the origin of the large  $k$  in the (Nd,Dy)-Fe-B sintered magnet is expected to facilitate the attainment of the physical limit of coercivity in all types of hard magnetic materials.

In this context, we investigated the microstructure of Dy-free and Dy-containing sintered magnets using scanning transmission electron microscopy (STEM) and atom probe tomography (APT) in combination with first-principles calculations and micromagnetic simulations, and we determined the microstructural origins of the large  $k$  for the partially Dy-substituted sintered magnet. The angular dependence of coercivity showed a change in the reversal mechanism by the partial substitution of Nd with Dy in Nd-Fe-B sintered magnets. Contrary to the conventional understanding that the coercivity increase was merely due to the increase in  $H_A$ , soft X-ray magnetic circular dichroism (XMCD) and first-principles calculations showed that a slight enrichment of Dy ( $\sim 4$  at.%) in the  $\sim 2$  nm-thick intergranular phase substantially reduced the magnetization, indicating an extrinsic origin of the coercivity increase as well. This additional extrinsic origin was supported by the change in the angular dependence of coercivity from the Kondorsky-type to the Stoner–Wohlfarth-type. Hence, the exceptionally high coercivity value of  $0.4H_A$  mainly originated from the

magnetization reduction of the intergranular phase in (Nd, Dy)-Fe-B sintered magnets by Dy alloying.

## Materials and methods

### Sample preparation, magnetic property measurement and microstructure characterization

The Dy-free and Dy-containing sintered magnets, with at.% compositions of  $\text{Nd}_{14.5}\text{Fe}_{78.1}\text{Co}_{1.0}\text{Cu}_{0.2}\text{B}_{6.2}$  and  $\text{Nd}_{10.8}\text{Dy}_{3.7}\text{Fe}_{78.1}\text{Co}_{1.0}\text{Cu}_{0.2}\text{B}_{6.2}$  (9 wt% Dy), were prepared by a conventional powder processing route. The green compacts were sintered at 1010–1040 °C for Dy-free magnets and 1050–1080 °C for Dy-containing magnets for 2–4 h, respectively. A higher sintering temperature was required for the densification of Dy-containing magnets. The annealing process was performed at 500–650 °C for 1–2 h. The room temperature and high-temperature magnetic properties were measured using a pulse *BH* tracer. The angular dependences of the coercivity were measured at various tilting angles of the easy axis on the tracer. Note that  $\mu_0 H_c(\theta)$  is defined as the field at which the maximal susceptibility ( $dM/dH$ ) is obtained in the demagnetization curve<sup>30</sup>. The general and detailed microstructure characterizations were carried out using a scanning electron microscope (SEM, Carl Zeiss Cross-Beam 1540 ESB) and an aberration-corrected transmission electron microscope (TEM, Titan G2 80-200), respectively. The samples for atom probe tomography were prepared by the lift-out technique using a G4-UX dual-beam system, and the atom probe experiments were carried out using a laser-assisted local electrode atom probe (CAMECA LEAP5000 XS). Atom probe tomography was conducted in laser mode at a specimen temperature of 50 K with a laser pulse energy of 30 pJ and pulse rate of 250 kHz. The atom probe results were analyzed using CAMECA Integrated Visualization and Analysis Software (IVAS®).

### XMCD measurements

To determine the Fe magnetic moment of the intergranular phase on the fractured surface, surface-sensitive soft XMCD spectra at the Fe  $L_{2,3}$ -edges were recorded at the BL25SU beamline in SPring-8. The measurements were conducted using rod-shaped samples, which were cut to dimensions of  $\sim 0.5 \times 0.5 \times 10 \text{ mm}^3$  with the magnetic easy-axis along the long dimension. Before the XMCD measurements, the samples were introduced to the sample preparation chamber of the XMCD measurement system, which was kept under a high vacuum condition ( $\sim 3 \times 10^{-6}$  Pa), and subsequently fractured along a plane perpendicular to the magnetic easy-axis inside to obtain a fresh surface. The fractured sample was immediately transferred to the main chamber, which was kept under ultrahigh vacuum ( $< 5 \times 10^{-7}$  Pa). The samples were heated to 200 °C and then cooled to room

temperature under a magnetic field of 1.9 T in the measurement system to saturate the magnetization of the samples. A magnetic field of 1.9 T was applied along the easy magnetization axis of the sample during the measurements. The XMCD signal ( $\mu_m$ ) was obtained as  $\mu_m = \mu_l - \mu_r$ , where  $\mu_r$  and  $\mu_l$  represent the X-ray absorption spectrum (XAS) for the helicity plus ( $h_+$ ) and minus ( $h_-$ ) of soft X-rays, respectively. The temperature dependence of the XMCD spectra was obtained during the heating processes. The degree of circular polarization was previously estimated as 0.96 at 400 eV<sup>39</sup> and was expected to be similar or larger in the energy region used in the present work. The angle between the magnetic field and incident X-ray beam was  $10^\circ$ <sup>40</sup>.

The magnetic moment of the intergranular phase was obtained with a modified calculation method based on the reference by Nakamura et al.<sup>41</sup> with an applied correction accounting for the regions where the exposed surface was not covered by the grain boundary (intragrain fractures):

$$m_{\text{XMCD}} = \frac{(1-f)(m_{\text{IGP}} W_{\text{IGP}} + m_{\text{NFB}} W_{\text{NFB}}) + f \lambda_e m_{\text{NFB}} c_{\text{NFB}}}{(1-f)(W_{\text{IGP}} + W_{\text{NFB}}) + f \lambda_e c_{\text{NFB}}}$$

$$W_{\text{IGP}} = \int_0^{t_{\text{IGP}}} c_{\text{IGP}} \exp\left(-\frac{z}{\lambda_e}\right) dz, \quad W_{\text{NFB}} = \int_{t_{\text{IGP}}}^{\infty} c_{\text{NFB}} \exp\left(-\frac{z}{\lambda_e}\right) dz$$

where  $m_{\text{XMCD}}$  is the calculated Fe magnetic moment from XMCD measurements,  $f$  is the estimated fraction of intragrain fracture surface,  $m_{\text{IGP}}$  is the magnetic moment of Fe in the intergranular phase,  $m_{\text{NFB}}$  is the magnetic moment of Fe in the  $\text{Nd}_2\text{Fe}_{14}\text{B}$  phase,  $\lambda_e$  is the probing depth (1.2 nm<sup>42</sup>),  $t_{\text{IGP}}$  is the thickness of the intergranular phase,  $c_{\text{IGP}}$  is the Fe concentration in the intergranular phase, and  $c_{\text{NFB}}$  is the Fe concentration for the stoichiometric composition of the  $\text{Nd}_2\text{Fe}_{14}\text{B}$  phase (0.82). The values of  $m_{\text{XMCD}}$  of the Fe magnetic moment were calculated by magneto-optical sum rule analysis for XMCD<sup>43–45</sup>, using the value for the number of 3d electrons of Fe as 6.67<sup>41</sup>. The temperature dependence of  $m_{\text{NFB}}$  was obtained from Mössbauer measurements by Kamal et al.<sup>45</sup> and was normalized to  $m_{\text{NFB}} = 2.27 \mu_B$  at RT, which was obtained from the XMCD experiment of a  $\text{Nd}_2\text{Fe}_{14}\text{B}$  single crystal by García et al.<sup>46</sup> The values of  $c_{\text{IGP}}$  and  $t_{\text{IGP}}$  were extracted from the TEM-EDS measurements. The areal fraction of the intragrain fracture ( $f$ ) was calculated from the XAS microscopy observations<sup>47</sup> of a total of 0.018 mm<sup>2</sup> and 0.0324 mm<sup>2</sup> for the Dy-free and Dy-containing magnets, respectively, with values of 5.67% and 11.92% for the Dy-free and Dy-containing magnets, respectively.

The XMCD microscopy observations were performed at room temperature on the soft X-ray beamline BL25SU, SPring-8. The measurement sample was prepared by the same method as the XMCD spectrum measurement

described above. The absorption signal was detected by the total electron yield (TEY) method at the Fe  $L_3$  edge (707.9 eV). This instrument had a focal depth of  $\pm 5 \mu\text{m}$  from the focal point with a spatial resolution of  $\sim 100 \text{ nm}$  and was equipped with a superconducting magnet with a maximum field of  $\pm 8 \text{ T}$ . Further technical details are described in references<sup>47,48</sup>. A total of 27 and 35 images were taken for the Dy-free and Dy-containing samples, respectively, between remanence and  $-4 \text{ T}$ , with field steps between  $0.05 \text{ T}$  and  $0.2 \text{ T}$ , respectively.

### First-principles calculations

Our first-principles calculations were based on density functional theory within the generalized gradient approximation<sup>49</sup> as implemented in the OpenMX code<sup>50</sup>. We adopted open-core pseudopotentials with three Nd 4f electrons as spin-polarized core states. As valence states, 3p states of Fe and 5s and 5p states of Nd were explicitly calculated. The convergence criteria for the force and the total energy were selected to be  $1.0 \times 10^{-3}$  Hartree/Bohr and  $1.0 \times 10^{-6}$  Hartree, respectively. The atomic structures of amorphous alloys were initially prepared by the melt quenching method based on first-principles molecular dynamics simulations with a time step of  $1 \text{ fs}$ <sup>51</sup>. We used supercells containing 54 atoms and compositions similar to  $\text{Nd}_x\text{Fe}_{92-x}\text{Co}_2\text{Cu}_6$  and  $\text{Nd}_{x-4}\text{Dy}_4\text{Fe}_{92-x}\text{Co}_2\text{Cu}_6$  ( $x = 42, 50, 54$ ). Then, structure optimization was performed using a  $7 \times 7 \times 7$   $k$ -point grid, a cutoff energy of  $500 \text{ Ry}$ , and the pseudoatomic orbital basis sets of  $s2p2d2$  for Fe, Co and Cu and  $s3p2d2$  for Nd and Dy. As the initial spin configuration, spin polarizations in transition metals and rare-earth metals were set as antiparallel. We used the average of five atomic configurations for each composition to account for the fluctuations in the magnetization due to the amorphous structures.

### Micromagnetic simulations

The model for micromagnetic simulations contained 125 polyhedron-shaped grains with an average grain size of  $\sim 100 \text{ nm}$ , which were separated by a  $3 \text{ nm}$  intergranular phase. The intrinsic properties of  $\text{Nd}_2\text{Fe}_{14}\text{B}$  grains at room temperature were assumed as follows: uniaxial anisotropy energy  $K_1 = 4.36 \text{ MJ m}^{-3}$  and exchange stiffness  $A = 8 \text{ pJ m}^{-1}$ <sup>37</sup>. The composition of the matrix 2-14-1 phase for Dy-containing magnets was measured to be approximately  $(\text{Nd}_{0.8}\text{Dy}_{0.2})_2\text{Fe}_{14}\text{B}$ . Based on this, the intrinsic properties of  $(\text{Nd}_{0.8}\text{Dy}_{0.2})_2\text{Fe}_{14}\text{B}$  were assumed to follow Vegard's law, with the following values:  $K_1 = 4.8 \text{ MJ m}^{-3}$  and  $A = 8.4 \text{ pJ m}^{-1}$ . In this work, we modified the properties of the intergranular phase and systematically investigated their influence on the angular dependences of coercivities. On the model surface, one grain was assumed to be a "defect grain" with reduced anisotropy energy,  $K_1^{\text{def}}$ . This assumption was validated

by experimental observations<sup>47,52</sup>. The simulation code "b4vex" was used to study the demagnetization process at a field step of  $\Delta\mu_0 H_z = -5 \text{ mT}$ . At each field, the free energy of the whole model was minimized via a conjugate gradient method with a modified line search<sup>53</sup>.

### Results

Figure 2a shows the demagnetization curves of the Dy-free and Dy-containing samples. A coercivity of  $1.28 \text{ T}$  with a remanence of  $1.46 \text{ T}$  was measured for the Dy-free magnet. The coercivity was substantially enhanced to  $3.32 \text{ T}$  in Dy-containing magnets. Moreover, the value of  $H_c/H_A$  substantially increased from  $0.19$  for the Dy-free magnet to  $0.40$  for the Dy-containing magnet, as shown in Fig. 1. The magnetic hardening mechanism of the samples was then investigated by measuring the angular dependence of coercivity ( $H_c(\theta)$ ), as shown in Fig. 2b. A monotonic increase in coercivity against the measurement angle was obtained for the Dy-free magnet. In contrast,

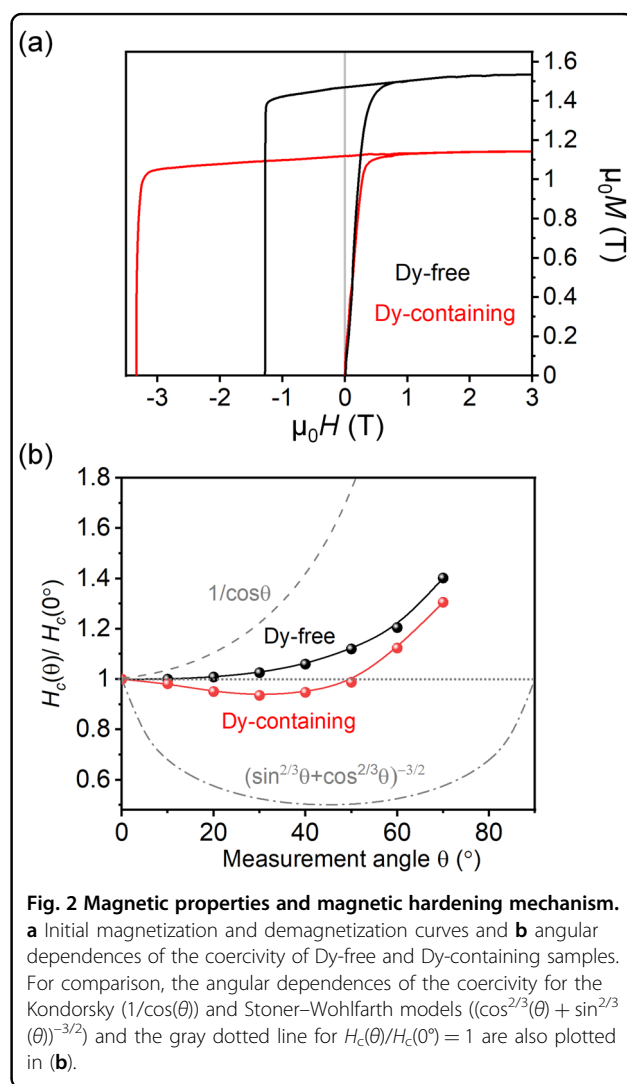


**Fig. 2** Magnetic properties and magnetic hardening mechanism. **a** Initial magnetization and demagnetization curves and **b** angular dependences of the coercivity of Dy-free and Dy-containing samples. For comparison, the angular dependences of the coercivity for the Kondorsky ( $1/\cos(\theta)$ ) and Stoner–Wohlfarth models ( $(\cos^{2/3}(\theta) + \sin^{2/3}(\theta))^{-3/2}$ ) and the gray dotted line for  $H_c(\theta)/H_c(0^\circ) = 1$  are also plotted in (b).

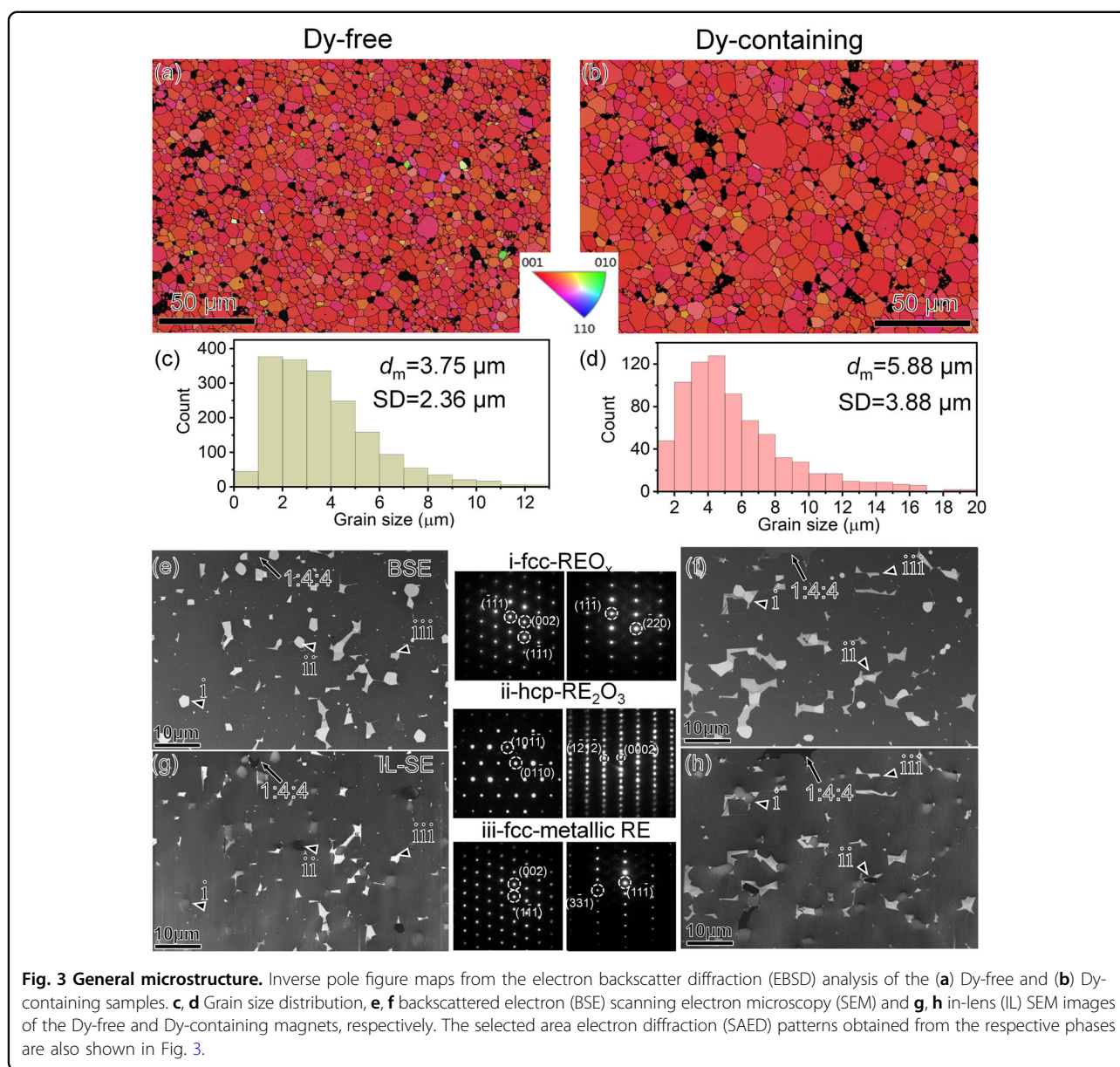
the coercivity for the Dy-containing magnet initially decreased with  $\theta$  and then increased after  $\theta > 30^\circ$ . Thus, a local minimum appeared on the  $H_c(\theta)$  curve for the Dy-containing magnet. Li et al. reported that the magnetism of the intergranular phase in Nd-rich Ga-doped Nd-Fe-B sintered magnets influenced the shape of the  $H_c(\theta)$  curve<sup>36</sup>. Notably, the shape of the  $H_c(\theta)$  curve for the Dy-containing magnet measured in this work was much closer to the ideal case of the Stoner–Wohlfarth model compared to that for Nd-rich Ga-doped sintered magnets with a  $k$  value of 0.25<sup>36</sup>; here, the  $\text{Nd}_2\text{Fe}_{14}\text{B}$  grains were claimed to be enveloped by the weak ferromagnetic intergranular phase containing only 10 at.% Fe as well as the anti-ferromagnetic  $\text{Nd}_6\text{Fe}_{13}\text{Ga}$  phases<sup>18,36,54</sup>. This comparison in  $H_c(\theta)$  indicated a possibly low magnetization of the intergranular phase in the Dy-containing sample. Another indication of the low magnetization of the intergranular phase could be found in the temperature dependence of the coercivity. Recent work by Li et al.<sup>55</sup> demonstrated that the change in the  $H_c$ - $T$  curve shape from concave to linear was ascribed to the reduction in the magnetization of the intergranular phase. In our study, the linear behavior of the  $H_c$ - $T$  curve could be observed for the Dy-containing sample in contrast to the concave shape for the Dy-free sample, as shown in the Supplementary Information. This additionally confirmed that the magnetization of the intergranular phase was reduced after alloying Dy into the magnet.

The overall microstructure is shown in Fig. 3. The inverse pole figure maps in Fig. 3a, b from the EBSD analysis of the Dy-free and Dy-containing samples indicated that the 2-14-1 grains were strongly textured along the [001] direction. Furthermore, the average grain size ( $d_m$ ) increased from 3.75  $\mu\text{m}$  (Dy-free sample) to 5.88  $\mu\text{m}$  (Dy-containing sample), as shown by the grain size distribution in Fig. 3c, d. The larger grain size was due to the higher sintering temperature required for the densification of Dy-containing magnets. This directly led to a reduction in the grain boundary fraction from 12.3 to 8.1% in the Dy-containing sample. The secondary phases mainly consisted of metallic *fcc*-RE, *hcp*- $\text{RE}_2\text{O}_3$ , and *fcc*- $\text{REO}_x$ . Moreover, the main Nd-rich phases were indexed by a combination of the backscattered electron (BSE) images, in-lens secondary electron (IL-SE) SEM images and selected area electron diffraction (SAED) images. From Fig. 3e–h, these two samples shared three different RE-rich phases. Phase i with bright contrast in the BSE image and gray contrast in the IL-SE SEM image is indexed to *fcc*- $\text{REO}_x$ . Next, phase ii was brightly imaged in the BSE image and darkly imaged in the IL-SE SEM image, which was identified as  $\text{La}_2\text{O}_3$ -type  $\text{RE}_2\text{O}_3$  (*hcp*) with a higher oxygen concentration. Last, phase iii with the brightest contrast in the IL-SE SEM image also showed brighter contrast compared to the 2-14-1 matrix

phase in the BSE image; this phase corresponded to the metallic RE-rich phase with an *fcc* crystal structure. Considering its RE-rich composition with respect to stoichiometry ( $\text{RE}_{11.76}\text{Fe}_{82.35}\text{B}_{5.88}$  at.%), the composition of  $\text{RE}_{14.5}\text{Fe}_{78.1}\text{Co}_{1.0}\text{Cu}_{0.2}\text{B}_{6.2}$  (at.%) in our study was within the (2:14:1 + liquid phase) two-phase region during the liquid-phase sintering process at temperatures above 1000 °C<sup>56</sup>. After the sintering process and during solidification, the metallic RE-rich phase was formed in the triple junctions. This phase in the triple junctions further diffused into the thin grain boundary after an optimal postsinter annealing process at 500–650 °C, leading to the formation of a uniform thin intergranular phase, as comprehensively discussed in ref. 57. Hence, the metallic RE-rich phase was beneficial to the coercivity enhancement, while the RE-oxide phase serves against the coercivity improvement. Overall, these phase identifications were consistent with previous literature<sup>38,58</sup>, and the role of the secondary phase on coercivity was discussed elsewhere<sup>58</sup>.

Figure 4a, b shows the APT for Nd+Cu and B obtained from the Dy-free sample and Nd + Cu and Dy for the Dy-containing sample, respectively. For both samples, the intergranular phase was enriched by Nd and Cu and depleted from B. The line concentration profiles obtained across the selected box perpendicular to the intergranular phase are shown in Fig. 4c, d for the Dy-free and Dy-containing samples, respectively. The compositions of the 2-14-1 matrix phase for the Dy-free and Dy-containing samples were determined from APT to be  $\text{Nd}_{12.13}\text{Fe}_{81.01}\text{Co}_{1.14}\text{B}_{5.72}$  (at.%) for Dy-free and  $\text{Nd}_{9.50}\text{Dy}_{2.67}\text{Fe}_{80.8}\text{Co}_{1.21}\text{B}_{5.82}$  (at.%) for Dy-containing magnets, which were similar to the compositions of  $\text{Nd}_2\text{Fe}_{14}\text{B}$  and  $(\text{Nd}_{0.78}\text{Dy}_{0.22})_2\text{Fe}_{14}\text{B}$ , respectively. Moreover, Dy was slightly enriched in the intergranular phase (3.87 at.%) compared to its concentration in the 2-14-1 matrix phase (2.67 at.%). Note that a larger evaporation field at the intergranular phase than that of the 2:14:1 matrix grain resulted in a reduction in the DC voltage while probing the intergranular phase at a fixed evaporation flux rate. Therefore, the DC voltage needed to be immediately increased again after reaching the adjacent 2:14:1 after probing the grain boundary region to maintain a fixed evaporation flux rate. This resulted in an artifact in a slight depletion of the constituent elements in the interface with the intergranular phase, as marked by the arrow head in Fig. 4a. However, this did not affect the fact that the B was depleted from the intergranular phase and the compositional analysis of the main phase.

Since boron was found to be absent in the intergranular phase, hereafter, the chemical composition in the intergranular phase was estimated by using STEM-EDS; this technique provided a better quantitative result by improving statistics via compositional analysis of several



intergranular phases for both magnets. The Supplementary Information contains the observations from several intergranular phases and their compositions for both samples. In the Dy-free sample, the composition of the intergranular phase parallel to the *c*-plane was determined to be 48.2 at.% Nd and 45.9 at.% Fe + Co. Meanwhile, the composition of Dy-containing sample was determined to be 53.6 at.% Nd and 37.7 at.% Fe + Co. This trend in the composition of the intergranular phase parallel to the *c*-plane intergranular phase was also observed in the *ab*-plane intergranular phase of the two samples. Specifically, we detected 35 at.% Nd and 62.1% Fe + Co for the Dy-free sample and 47.4 at.% Nd and 45.1 at.% Fe + Co in the *ab*-plane intergranular phase of the Dy-containing sample. The compositions

averaged from several intergranular phases, including *c*-plane and *ab*-plane intergranular phases, are summarized in Table 1. In addition, the composition of the matrix phase was determined to be  $(\text{Nd}_{0.81}\text{Dy}_{0.19})_2\text{Fe}_{14}\text{B}$ , and ~3–4 at.% Dy was found in the intergranular phase of the Dy-containing sample; this result was in good agreement with the APT results. Figure 4e, f shows representative high-resolution and high-angle annular dark-field (HAADF)-STEM images taken at the *c*-plane and *ab*-plane interfaces of two  $\text{RE}_2\text{Fe}_{14}\text{B}$  grains, along with the compositional line profiles obtained across the Nd-rich intergranular phases in the Dy-free and Dy-containing samples. The amorphous intergranular phase enriched with RE were clearly observed from high-resolution

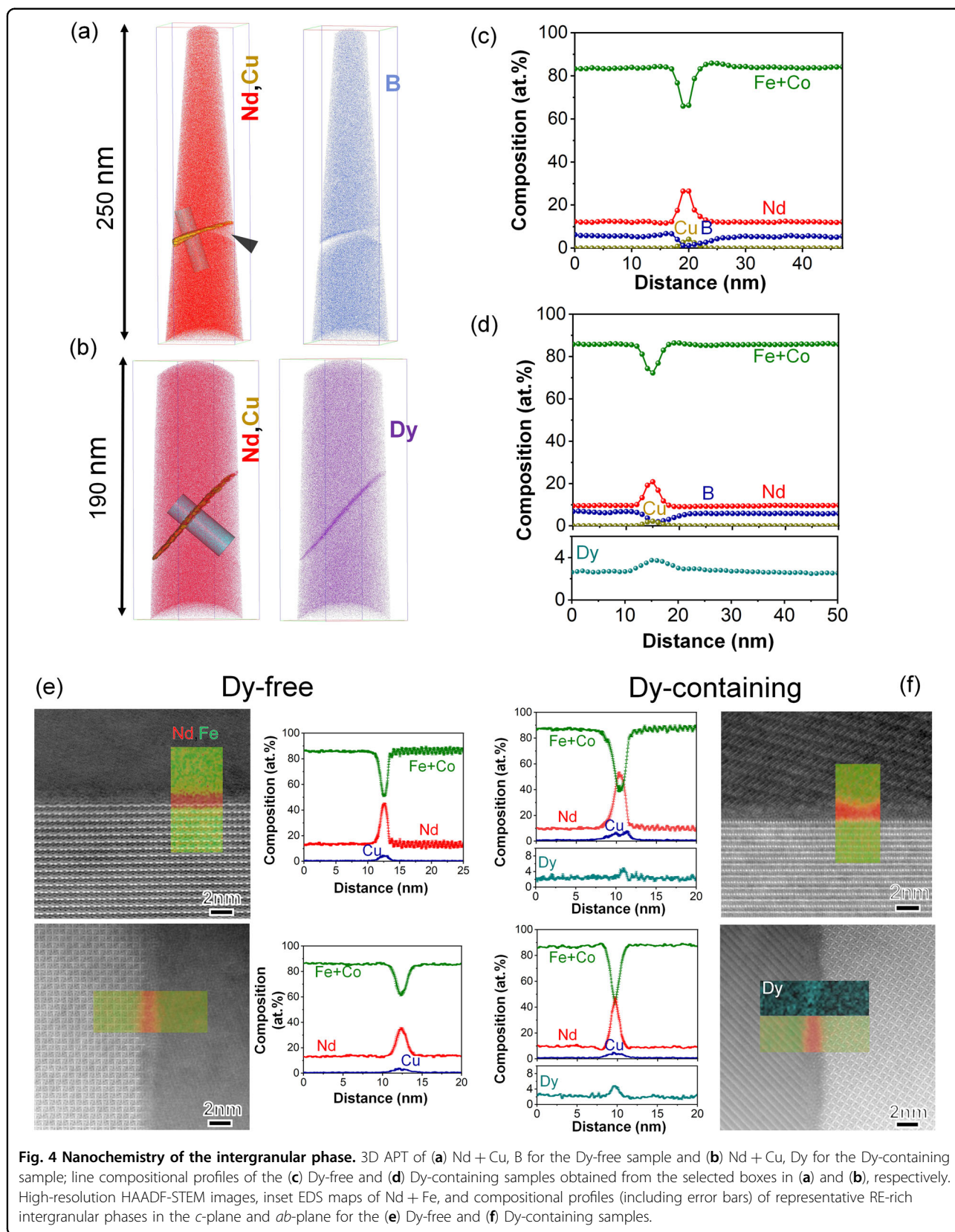


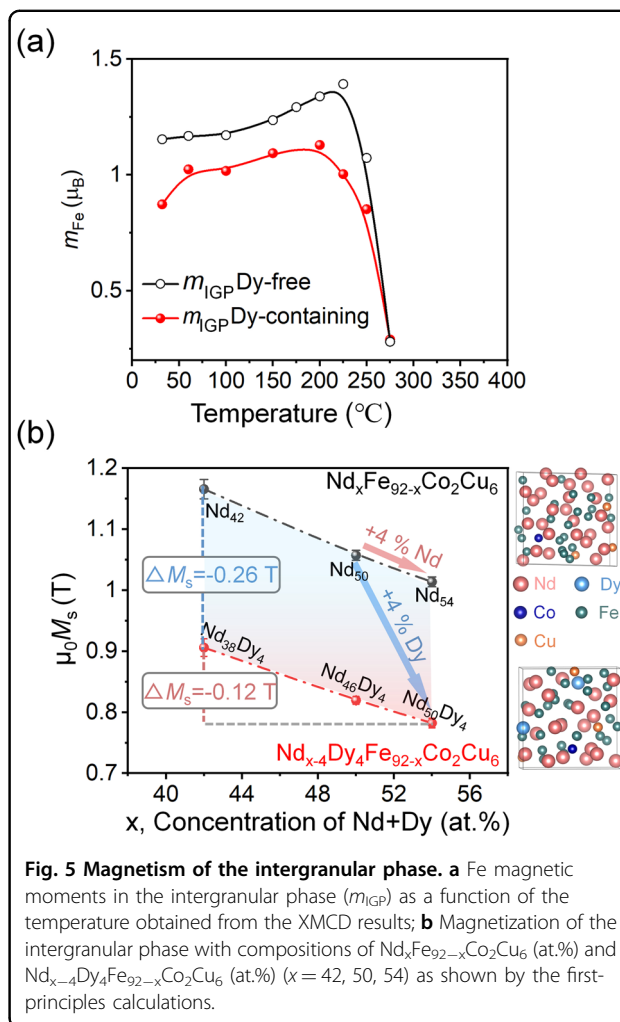
**Fig. 4** Nanochemistry of the intergranular phase. 3D APT of (a) Nd + Cu, B for the Dy-free sample and (b) Nd + Cu, Dy for the Dy-containing sample; line compositional profiles of the (c) Dy-free and (d) Dy-containing samples obtained from the selected boxes in (a) and (b), respectively. High-resolution HAADF-STEM images, inset EDS maps of Nd + Fe, and compositional profiles (including error bars) of representative RE-rich intergranular phases in the *c*-plane and *ab*-plane for the (e) Dy-free and (f) Dy-containing samples.

**Table 1** Summary of the average composition of the intergranular phase for Dy-free and Dy-containing samples.

Sample	Nd (at.%)	Dy (at.%)	Fe (at.%)	Co (at.%)	Cu (at.%)
Dy-free	41.57 ± 6.92	0	51.89 ± 8.01	2.12 ± 0.44	4.24 ± 1.67
Dy-containing	50.03 ± 6.01	3.90 ± 0.82	38.04 ± 6.60	1.98 ± 0.49	6.0 ± 1.65

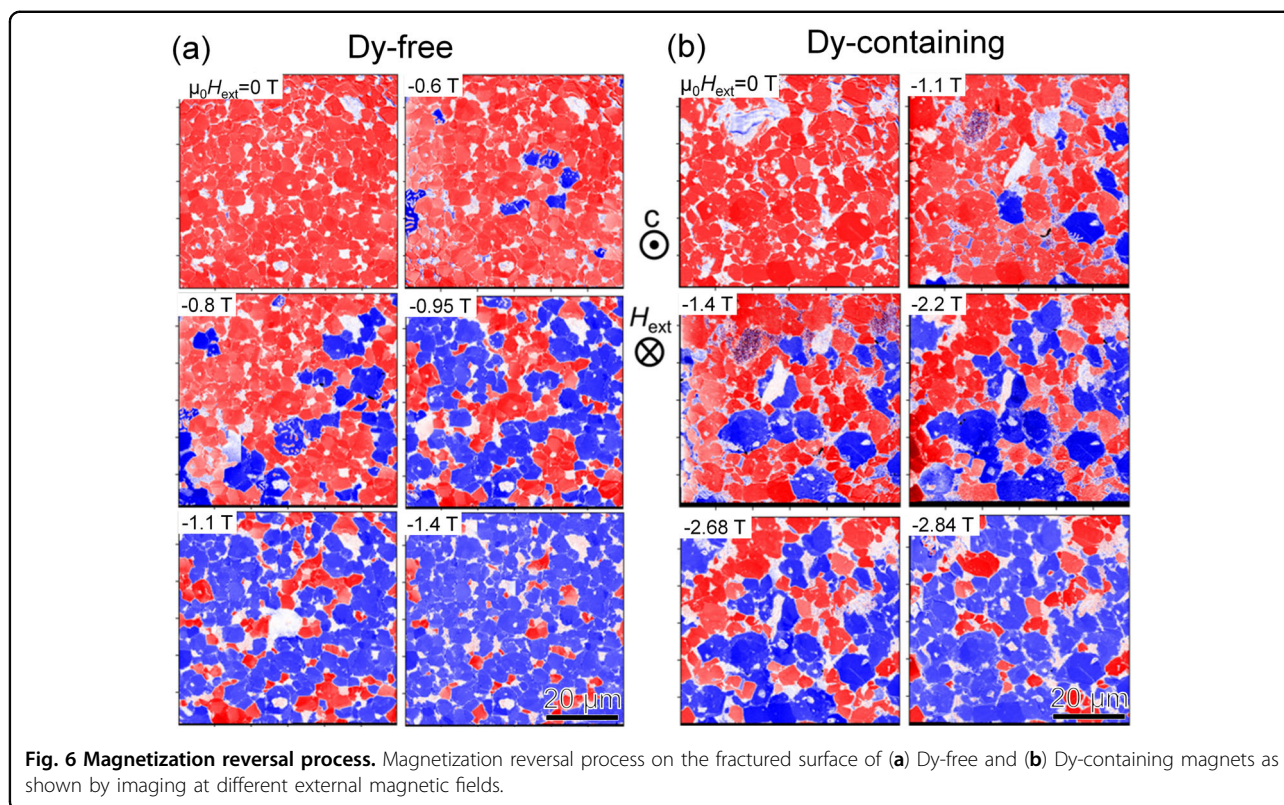
HAADF-STEM images. Moreover, the Dy-enriched intergranular phase was also observed in some cases, wherein the intensity of Dy was stronger in the intergranular phase than in the 2-14-1 phase (Fig. 4f). The above results clearly showed that the RE concentration in the intergranular phase for the Dy-containing sample was higher than that for the Dy-free sample. This result could be explained by the larger grain size and the resulting smaller fraction of intergranular phase for the given total RE concentration (14.5 at.%) in the Dy-containing magnet, as shown in Fig. 3.

Herein, we discuss the influence of Dy in the intergranular phase on its magnetism. Figure 5a shows the temperature dependence of the Fe magnetic moments of the intergranular phase measured by XMCD. The Fe magnetic moment of the intergranular phase,  $m_{\text{Fe}}$ , was lower for the Dy-containing sample than for the Dy-free sample in the temperature range of 32–225 °C. Note that Fe was the main ferromagnetic element in the intergranular phase of both samples, which can define its magnetization at room temperature. A sharp decrease in the magnetization of the intergranular phase,  $m_{\text{IGP}}$ , was observed at 275 °C for both samples, indicating a comparable Curie temperature of the intergranular phase for both Dy-free and Dy-containing samples. The possible origin for the lower  $m_{\text{Fe}}$  of the Dy-containing sample could be the nature of exchange coupling between Dy and Fe, which was typically anti-ferromagnetic in the crystalline structure, reducing the magnetization of the intergranular phase from 1.15  $\mu_{\text{B}}$  to 0.87  $\mu_{\text{B}}$  at room temperature, as shown in Fig. 5a. Here, the effect of the composition of the intergranular phase on its magnetization was further investigated by first-principles calculations using the compositions of  $\text{Nd}_x\text{Fe}_{92-x}\text{Co}_2\text{Cu}_6$  and  $\text{Nd}_{x-4}\text{Dy}_4\text{Fe}_{92-x}\text{Co}_2\text{Cu}_6$  ( $x = 42, 50, 54$ ). We considered five different atomic arrangements for the amorphous intergranular phase of Dy-free and Dy-containing samples, and two examples of supercells for this calculation are shown in Fig. 5b. The amorphous nature of the intergranular phase was statistically confirmed by TEM observations, as shown in the Supplementary Information. The calculated magnetization for the intergranular phase,  $m_{\text{IGP}}$ , for the Dy-free and Dy-containing samples is shown in Fig. 5b, wherein the magnetization of the intergranular phase was reduced by  $\sim 0.25$  T with only 4 at.% Dy for different  $x$  values. For the experimentally determined compositions of



$\text{Nd}_{42}\text{Fe}_{50}\text{Co}_2\text{Cu}_6$  (at.%) and  $\text{Nd}_{50}\text{Dy}_4\text{Fe}_{38}\text{Co}_2\text{Cu}_6$  (at.%) for Dy-free and Dy-containing magnets, respectively, as shown in Table 1. The magnetization of the intergranular phase was reduced from 1.17 T for the Dy-free magnet to 0.78 T for the Dy-containing magnet, due to the anti-ferromagnetic coupling between Dy and Fe; It can be seen that a magnetization reduction of 0.26 T was achieved with 4 at.% Dy, while the magnetization was reduced by only 0.12 T with 8 at.% Nd. Thus, the lower magnetization of IGP in Dy-containing magnets was not only due to the lower Fe concentration but also, more importantly, due to the anti-ferromagnetic coupling between Dy and Fe. Note that there was comparable Cu

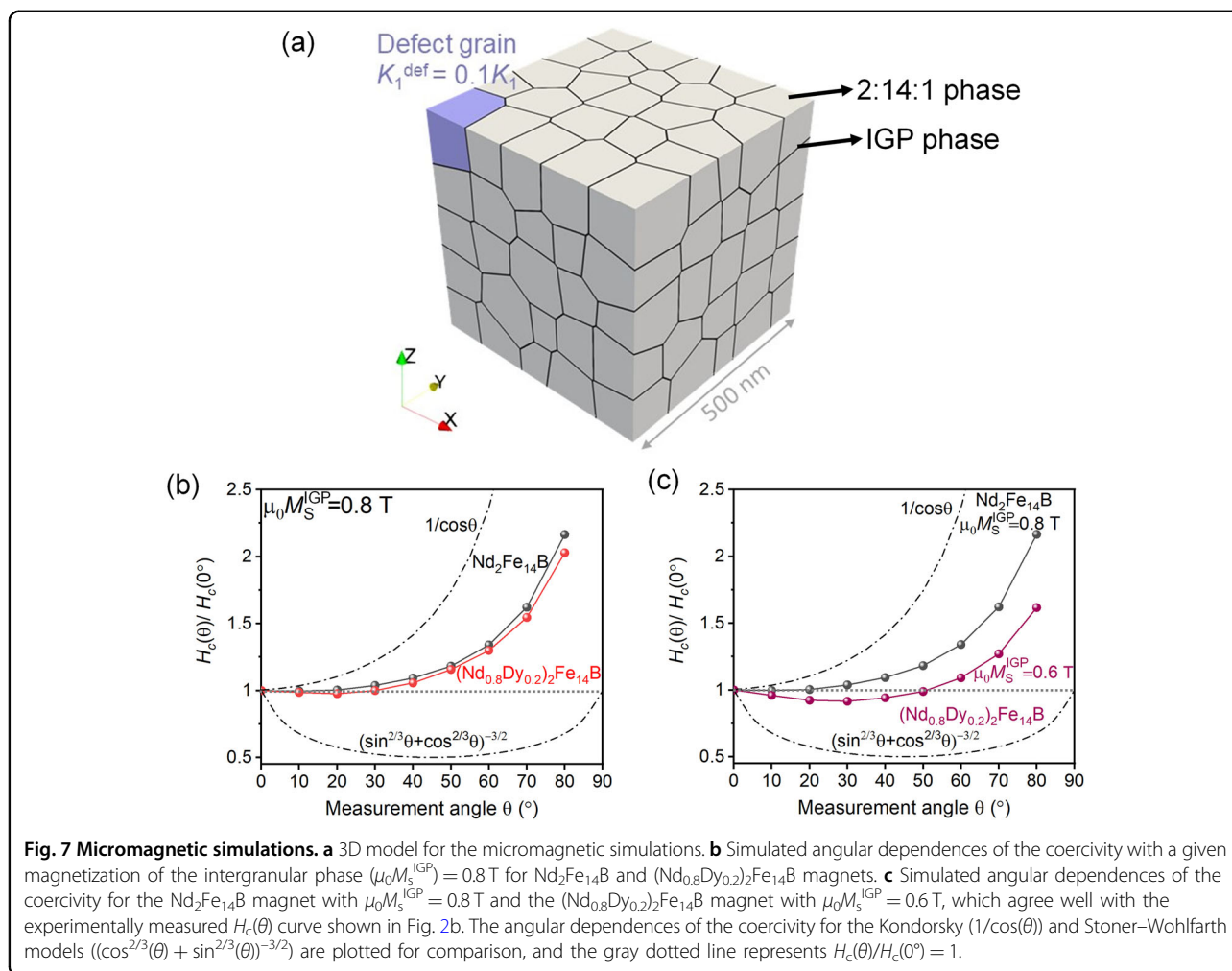




segregation in the intergranular phase of both Dy-free and Dy-containing samples with a minor difference within statistical error, as shown in Table 1. Cu had no magnetic moment and could only slightly dilute the magnetization of the intergranular phase. Overall, the  $m_{IGP}$  values of both samples calculated by the first-principles method were in good agreement with the experimental values from XMCD.

Figure 6 shows the evolution of magnetic domains at the fractured surfaces of the two magnets under an external magnetic field during the demagnetization process probed by soft XMCD microscopy. The samples for XMCD imaging did not have to have a mirror surface; thus, the magnetic domain images on the fractured surface covered by the intergranular phase were observed by varying external magnetic fields<sup>41</sup>. The Dy-free and Dy-containing samples were saturated at 4 T and 6 T magnetic fields respectively, followed by a reduction of the magnetic field to 0 T. The magnetic domain patterns of a remanent magnetization state and their dynamics during the magnetization reversal process are shown in Fig. 6. The grains with red contrast indicated a persistent saturation state after releasing the external field ( $\mu_0 H_{ext} = 0$  T) because of good texture. After applying  $-0.6$  T to the Dy-free sample, magnetization reversal occurred by the formation of multidomain structures. Decreasing the field to  $-0.8$  T led to the further nucleation

and propagation of reversed magnetic domains. With a slight decrease in the field from  $-0.8$  T to  $-0.95$  T, a cascade propagation of reversed domains resulted in the presence of a large areal fraction of reversed domains with blue contrast due to the weak pinning strength of the intergranular phase against magnetic domain wall propagation. For the Dy-containing sample shown in Fig. 6b, decreasing the magnetic field to  $-1.1$  T led to the nucleation of reversed magnetic domains in the large grains. Moreover, the nucleation field for the Dy-containing sample was much larger than that of the Dy-free sample because of the increased  $H_A$  of the  $(Nd_{0.8}Dy_{0.2})_2Fe_{14}B$  grains. An external magnetic field down to  $-1.4$  T led to more nucleation and propagation of reversed magnetic domains. The magnetic domain structure strongly resisted the reversal until a large demagnetization magnetic field of  $-2.2$  T was applied. This result indicated that the intergranular phase in the Dy-containing magnet strongly prevented the propagation of reversed domains to the neighboring grains. Therefore, unlike the Dy-free sample, cascade domain wall propagation was not observed in the Dy-containing sample, and the magnetization reversal process proceeded only in a few grains next to the grains with reversed magnetic domains under a magnetic field of  $-2.68$  T. The magnetic hardening mechanism was defined according to the demagnetization process. Hence, the distinct difference in



the pinning strength of the intergranular phase against the demagnetization process of samples was additional evidence for the different magnetic hardening mechanisms, which agreed with the results on the angular dependence of the coercivity shown in Fig. 2b.

The influence of the intergranular phase magnetization on the angular dependences of the coercivity of both samples was investigated by micromagnetic simulations, as shown in Fig. 7. The contribution of the  $H_A$  of the matrix phase and the magnetism of the intergranular phase was independently calculated, as shown in the Supplementary Information. With the reduction of  $m_{\text{IGP}}$  from 0.8 T to 0.5 T for the Dy-free and Dy-containing samples, we clearly observed a change in  $H_c(\theta)$  curve shape from monotonically increasing to having a local minimum. This result indicated that the coercivity mechanism changed from the Kondorsky type to the weakly Stoner–Wohlfarth type by the dilution of magnetization in the intergranular phases<sup>35,36</sup>. Figure 7b compares the angular dependences of the coercivity for the Dy-free and Dy-containing samples with  $\mu_0 M_s^{\text{IGP}} = 0.8 \text{ T}$ . The shape of the  $H_c(\theta)$  curve did not

change, but its slope became slightly less steep in the Dy-containing sample. In other words, the increase in the anisotropy field in the matrix 2-14-1 phase by alloying with Dy suppressed the monotonic upward feature of  $H_c(\theta)$ , but its effect was limited. Figure 7c shows the simulated  $H_c(\theta)$  curve with  $\mu_0 M_s^{\text{IGP}} = 0.8 \text{ T}$  for the Dy-free sample and  $\mu_0 M_s^{\text{IGP}} = 0.6 \text{ T}$  for the Dy-containing sample, which reproduced the experimental data for  $0^\circ < \theta < 70^\circ$  given in Fig. 2b. Our micromagnetic simulations showed that the intergranular phase played a major role in the angular dependence of coercivity rather than the chemical composition of the matrix grains or  $H_A$ . Moreover, the  $m_{\text{IGP}}$  value for simulated  $H_c(\theta)$  in the Dy-containing sample agreed well with the experimental results shown in Fig. 5.

## Discussion

The development of high coercivity Nd-Fe-B-based magnets with a large energy density has been a long-standing goal in the study of permanent magnets. Previously, the coercivity of Nd-Fe-B sintered magnets was believed to be controlled by the nucleation of reversed

domains from weak points in the polycrystalline microstructure based on the high susceptibility in the initial magnetization curve and the abrupt reversal in the demagnetization process<sup>3,10</sup>. However, recent work on submicron-sized sintered<sup>34</sup> and hot-deformed magnets<sup>14</sup> clearly showed the feature of domain wall pinning in the initial magnetization curves. Using magneto-optic Kerr effect (MOKE) imaging during the demagnetization process, Soderžnik et al. detected distinct changes in the demagnetization process when the uniform intergranular phase was formed in Ga-containing Nd-Fe-B sintered magnets<sup>59</sup>. Numerous works have unequivocally demonstrated that the coercivity has a strong correlation with the magnetization of the intergranular phase,  $m_{IGP}$ <sup>13–19,41,60</sup>, which can be controlled by the chemical composition of the intergranular phase. A high RE concentration and a low Fe concentration lead to a reduction in  $m_{IGP}$  and a strengthened pinning force against the propagation of the domain wall of the reversed region, hence increasing the coercivity. This can be experimentally achieved with an increase in the Nd concentration in the intergranular phase by increasing the total rare earth content in the alloy composition or by the grain boundary diffusion process<sup>13–19,23–25</sup>. In this work, we have shown that the slight enrichment of Dy (~4 at.%) in the intergranular phase substantially reduced its magnetization because of the anti-ferromagnetic coupling of Dy with Fe, even with a considerably large content of Fe in the intergranular phase. The modification of the magnetism of the 2 nm-thin intergranular phase caused the transition from the Kondorsky-type to Stoner–Wohlfarth-like behavior in the angular dependence of coercivity by weakening the intergranular exchange coupling. As a result, the coercivity ratio  $k$  substantially increased from 0.2 to 0.4. This change was reproduced by the micromagnetic simulation with different magnetism in the intergranular phase.

The APT and STEM-EDS analysis (Fig. 4) showed that the chemical composition of the matrix phase of the Dy-containing magnet was  $(Nd_{0.8}Dy_{0.2})_2Fe_{14}B$ . The anisotropy field of this 2-14-1 phase was estimated to be 8.4 T assuming that  $H_A$  showed a linear change between  $Nd_2Fe_{14}B$  and  $Dy_2Fe_{14}B$ <sup>37</sup>, which was also supported by experimental measurements in the Supplementary Information. If  $k = 0.2$ , as commonly observed in commercial sintered magnets, a coercivity of ~1.7 T was expected. However, the coercivity ratio of the Dy-containing magnet was found to be 0.4, which was twice as large as that (0.19) for the Dy-free sample. This coercivity enhancement could not be explained by only considering the intrinsic factor. Here, we noted that the change in the angular dependence of the coercivity clearly indicated a change in the magnetic hardening mechanism from the Kondorsky type (domain wall pinning) for the Dy-free magnet to the

one with the Stoner–Wohlfarth feature for the Dy-containing sample. Recently, Li et al.<sup>36</sup> demonstrated that the reduction of  $m_{IGP}$  by the formation of a weak ferromagnetic intergranular phase with 10 at.% ferromagnetic elements in Nd-Fe-B-based sintered magnets could suppress the monotonically increasing coercivity against the measurement angle. Based on a one-dimensional hard/soft/hard composite micromagnetic model, Li et al.<sup>33</sup> showed that the two types of angular dependences of the coercivity with or without a local minimum appeared depending on the ratio of the magnetizations between the hard phase and soft intergranular phase. The appearance or absence of a local minimum was confirmed as a sign of whether the switching was dominated by the spin rotation (nucleation of reversed domains) or by the depinning of the domain wall. In this work, however, the complete elimination of the ferromagnetic elements from the intergranular phase was not possible considering the tie lines between the  $Nd_2Fe_{14}B$  and the liquid phase<sup>56</sup>. Our new findings established that the magnetism of the intergranular phase could be reduced by a slight enrichment of Dy that anti-ferromagnetically couples with Fe even when the intergranular phase still contained a large content of ferromagnetic elements, such as Fe. This phenomenon increased the coercivity to  $0.4H_A$ , much larger than the conventional coercivity of  $0.2H_A$ , via a change in its magnetic hardening mechanism, as demonstrated by the angular dependence of coercivity and micromagnetic simulations.

## Conclusion

We investigated the magnetic hardening mechanism for (Nd, Dy)-Fe-B sintered magnets by a thorough microstructural characterization combined with measurements of the angular dependence of the coercivity and compared the results to those for the case for Nd-Fe-B sintered magnets. The results were interpreted based on finite element micromagnetic simulations using the experimentally determined parameters. A slight enrichment of Dy in the intergranular phase of the Dy-containing alloy reduced the magnetization by 25%, as shown by the XMCD measurements and first-principles calculations. This resulted in a large coercivity of  $0.4H_A$  in the (Nd,Dy)-Fe-B sintered magnets in contrast to  $0.2H_A$  for the Nd-Fe-B sintered magnet. Furthermore, the angular dependences of the coercivity indicated a change in the magnetic hardening mechanism from the Kondorsky model for the Nd-Fe-B magnet to the Stoner–Wohlfarth-like model for the (Nd, Dy)-Fe-B magnet. This occurred because the magnetization of the intergranular phase was substantially reduced due to the anti-ferromagnetic coupling of Fe and Dy ions. Our findings provide new insights into the microstructure design of Nd-Fe-B magnets. For instance,

the partitioning of an element that can anti-ferromagnetically couple with Fe within the inter-granular phase may lead to high coercivity in Nd-Fe-B magnets without relying on expensive Dy.

#### Acknowledgements

This work was supported by the Elements Strategy Initiative Center for Magnetic Materials (ESICMM), Grant Number JPMXP0112101004, through the Ministry of Education, Culture, Sports, Science and Technology (MEXT). The synchrotron radiation experiments were performed at BL25SU of Spring-8 with the approval of the Japan Synchrotron Radiation Research Institute (JASRI) (Proposal Nos. 2020A1785, 2020A1787, 2020A2046). Part of the first-principles calculations were carried out by using supercomputers at ISSP, The University of Tokyo, and TSUBAME, Tokyo Institute of Technology. H.S.-A. and T.N. acknowledge support from the NIMS-TOHOKU joint research partnership program. X.T. acknowledges the provision of an ICYS fellowship.

#### Author details

<sup>1</sup>National Institute for Materials Science, Tsukuba 305-0047, Japan.

<sup>2</sup>International Center for Young Scientists, National Institute for Materials Science, Tsukuba 305-0047, Japan. <sup>3</sup>International Center for Synchrotron Radiation Innovation Smart (SRIS), Tohoku University, Sendai 980-8577, Japan.

<sup>4</sup>Japan Synchrotron Radiation Research Institute, SPring-8, 1-1-1 Kouto, Sayo 679-5198, Japan. <sup>5</sup>Research Organization for Information Science and Technology, 6F, Kobe KIMEC Center Building, 1-5-2, Kobe 650-0047, Japan.

<sup>6</sup>Department of Materials Science and Engineering, Tokyo Institute of Technology, Yokohama 226-8502, Japan

#### Author contributions

X.T., J.L. and H.S.A. conceptualized and carried out the measurements of magnetic properties. X.T. and H.S.A. conducted general and detailed microstructure analysis. J.L. and A.B. contributed to the micromagnetic simulations. K.H. and H.S.A. supervised the project. A.M.C., S.K., Y.K., M.S. and T.N. performed XMCD measurements and analyzed the XMCD results. Y.G. and A.T. conducted first principle calculations. X.T., J.L. and H.S.A. interpreted the key findings and wrote the manuscript. All authors contributed to the discussions on the results and finalizing the manuscript.

#### Conflict of interest

The authors declare no competing interests.

#### Publisher's note

Springer Nature remains neutral with regard to jurisdictional claims in published maps and institutional affiliations.

**Supplementary information** The online version contains supplementary material available at <https://doi.org/10.1038/s41427-023-00498-5>.

Received: 11 November 2022 Revised: 5 August 2023 Accepted: 11 August 2023.

Published online: 29 September 2023

#### References

- Gutfleisch, O. et al. Magnetic materials and devices for the 21st century: stronger, lighter, and more energy efficient. *Adv. Mater.* **23**, 821–842 (2011).
- Croat, J. J., Herbst, J. F., Lee, R. W. & Pinkerton, F. E. High-energy product Nd-Fe-B permanent magnets. *Appl. Phys. Lett.* **44**, 148–149 (1984).
- Sagawa, M., Fujimura, S., Togawa, N., Yamamoto, H. & Matsuura, Y. New material for permanent magnets on a base of Nd and Fe (invited). *J. Appl. Phys.* **55**, 2083–2087 (1984).
- Sugimoto, S. Current status and recent topics of rare-earth permanent magnets. *J. Phys. Appl. Phys.* **44**, 064001 (2011).
- Hono, K. & Sepehri-Amin, H. Strategy for high-coercivity Nd-Fe-B magnets. *Scr. Mater.* **67**, 530–535 (2012).
- Brown, W. F. Virtues and weaknesses of the domain concept. *Rev. Mod. Phys.* **17**, 15 (1945).
- Brown, W. F. Relaxational behavior of fine magnetic particles. *J. Appl. Phys.* **30**, S130–S132 (1959).
- Hirosawa, S. et al. The dependence of coercivity on anisotropy field in sintered R-Fe-B permanent magnets. *J. Magn. Magn. Mater.* **61**, 363–369 (1986).
- Herzer, G., Fernengel, W. & Adler, E. On the theory of nucleation fields in uniaxial ferromagnets. *J. Magn. Magn. Mater.* **58**, 48–54 (1986).
- Kronmüller, H., Durst, K.-D. & Sagawa, M. Analysis of the magnetic hardening mechanism in RE-FeB permanent magnets. *J. Magn. Magn. Mater.* **74**, 291–302 (1988).
- Fischbacher, J. et al. Searching the weakest link: demagnetizing fields and magnetization reversal in permanent magnets. *Scr. Mater.* **154**, 253–258 (2018).
- Kronmüller, H. The nucleation fields of uniaxial ferromagnetic crystals. *Phys. Status Solidi B* **130**, 197–203 (1985).
- Liu, J. et al. Effect of Nd content on the microstructure and coercivity of hot-deformed Nd-Fe-B permanent magnets. *Acta Mater.* **61**, 5387–5399 (2013).
- Liu, J. et al. Grain size dependence of coercivity of hot-deformed Nd-Fe-B anisotropic magnets. *Acta Mater.* **82**, 336–343 (2015).
- Tang, X. J. et al. Coercivities of hot-deformed magnets processed from amorphous and nanocrystalline precursors. *Acta Mater.* **123**, 1–10 (2017).
- Tang, X., Sepehri-Amin, H., Ohkubo, T. & Hono, K. Suppression of non-oriented grains in Nd-Fe-B hot-deformed magnets by Nb doping. *Scr. Mater.* **147**, 108–113 (2018).
- Sepehri-Amin, H., Ohkubo, T. & Hono, K. The mechanism of coercivity enhancement by the grain boundary diffusion process of Nd-Fe-B sintered magnets. *Acta Mater.* **61**, 1982–1990 (2013).
- Sasaki, T. T. et al. Formation of non-ferromagnetic grain boundary phase in a Ga-doped Nd-rich Nd-Fe-B sintered magnet. *Scr. Mater.* **113**, 218–221 (2016).
- Sasaki, T. T. et al. Role of Ga on the high coercivity of Nd-rich Ga-doped Nd-Fe-B sintered magnet. *J. Alloy. Compd.* **790**, 750–759 (2019).
- Chen, B. et al. The mechanism of enhanced magnetic properties of sintered permanent magnets by substitution of Pr for Nd. *J. Alloy. Compd.* **516**, 73–77 (2012).
- Faria, R. N. The influence of zirconium addition and process parameters on the magnetic properties of Pr-Fe-B sintered magnets. *J. Magn. Magn. Mater.* **238**, 56–64 (2002).
- Tang, X., Lai, J., Sepehri-Amin, H., Ohkubo, T. & Hono, K. (Pr<sub>0.75</sub>Ce<sub>0.25</sub>)-Fe-B hot-deformed magnets for cryogenic applications. *Scr. Mater.* **194**, 113648 (2021).
- Sepehri-Amin, H. et al. High-coercivity ultrafine-grained anisotropic Nd-Fe-B magnets processed by hot deformation and the Nd-Cu grain boundary diffusion process. *Acta Mater.* **61**, 6622–6634 (2013).
- Liu, L. et al. Coercivity enhancement of Nd-Fe-B hot-deformed magnets by the eutectic grain boundary diffusion process using Nd-Ga-Cu and Nd-Fe-Ga-Cu alloys. *AIP Adv.* **8**, 056205 (2018).
- Tang, X. et al. Relationship between the thermal stability of coercivity and the aspect ratio of grains in Nd-Fe-B magnets: experimental and numerical approaches. *Acta Mater.* **183**, 408–417 (2020).
- Une, Y. & Sagawa, M. Presented at the 21st Workshop on Rare-Earth Permanent Magnets and Their Applications (Bled, Slovenia, 2010).
- Xu, X. D. et al. Origin of the coercivity difference in Nd-Fe-B sintered magnets processed from hydrogenation-disproportionation-desorption-recombination powder and jet-milled powder. *Acta Mater.* **151**, 293–300 (2018).
- Durst, K.-D. & Kronmüller, H. The coercive field of sintered and melt-spun NdFeB magnets. *J. Magn. Magn. Mater.* **68**, 63–75 (1987).
- Ramesh, R. & Srikrishna, K. Magnetization reversal in nucleation controlled magnets. I. *Theory J. Appl. Phys.* **64**, 6406–6415 (1988).
- Givord, D., Tenaud, P. & Viadieu, T. Angular dependence of coercivity in sintered magnets. *J. Magn. Magn. Mater.* **72**, 247–252 (1988).
- Givord, D., Lu, Q., Rossignol, M. F., Tenaud, P. & Viadieu, T. Experimental approach to coercivity analysis in hard magnetic materials. *J. Magn. Magn. Mater.* **83**, 183–188 (1990).
- Cebollada, F., Rossignol, M. F., Givord, D., Villas-Boas, V. & González, J. M. Angular dependence of coercivity in Nd-Fe-B sintered magnets: proof that coherent rotation is not involved. *Phys. Rev. B* **52**, 13511–13518 (1995).
- Li, J., Sepehri-Amin, H., Ohkubo, T. & Hono, K. Identifying the mechanism of hard magnet coercivity by its angular dependence. *Phys. Rev. B* **105**, 174432 (2022).
- Sepehri-Amin, H., Une, Y., Ohkubo, T., Hono, K. & Sagawa, M. Microstructure of fine-grained Nd-Fe-B sintered magnets with high coercivity. *Scr. Mater.* **65**, 396–399 (2011).

35. Bance, S. et al. Influence of defect thickness on the angular dependence of coercivity in rare-earth permanent magnets. *Appl. Phys. Lett.* **104**, 182408 (2014).
36. Li, J. et al. Angular dependence and thermal stability of coercivity of Nd-rich Ga-doped Nd-Fe-B sintered magnet. *Acta Mater.* **187**, 66–72 (2020).
37. Hirosawa, S. et al. Magnetization and magnetic anisotropy of  $R_2Fe_{14}B$  measured on single crystals. *J. Appl. Phys.* **59**, 873–879 (1986).
38. Vasilenko, D. Y. et al. Magnetic hysteresis properties and microstructure of high-coercivity (Nd,Dy)-Fe-B magnets with Dy less than 10 wt % and low oxygen. *Phys. Met. Metallogr.* **123**, 145–154 (2022).
39. Hirono, T., Kimura, H., Muro, T., Saitoh, Y. & Ishikawa, T. Full polarization measurement of SR emitted from twin helical undulators with use of Sc/Cr multilayers at near 400 eV. *J. Electron Spectrosc. Relat. Phenom.* **144–147**, 1097–1099 (2005).
40. Nakamura, T. et al. Development of a soft X-ray magnetic circular dichroism spectrometer using a 1.9T electromagnet at BL255U of SPring-8. *J. Electron Spectrosc. Relat. Phenom.* **144–147**, 1035–1038 (2005).
41. Nakamura, T. et al. Direct observation of ferromagnetism in grain boundary phase of Nd-Fe-B sintered magnet using soft x-ray magnetic circular dichroism. *Appl. Phys. Lett.* **105**, 202404 (2014).
42. Frazer, B. H., Gilbert, B., Sonderegger, B. R. & De Stasio, G. The probing depth of total electron yield in the sub-keV range: TEY-XAS and X-PEEM. *Surf. Sci.* **537**, 161–167 (2003).
43. Thole, B. T., Carra, P., Sette, F. & van der Laan, G. X-ray circular dichroism as a probe of orbital magnetization. *Phys. Rev. Lett.* **68**, 1943–1946 (1992).
44. Chen, C. T. et al. Experimental confirmation of the X-ray magnetic circular dichroism sum rules for iron and cobalt. *Phys. Rev. Lett.* **75**, 152–155 (1995).
45. Kamal, R. & Andersson, Y. Mössbauer spectroscopic studies of  $Nd_2Fe_{14}B$ . *Phys. Rev. B* **32**, 1756–1761 (1985).
46. García, L. M., Chaboy, J., Bartolomé, F. & Goedkoop, J. B. Orbital magnetic moment instability at the spin reorientation transition of  $Nd_2Fe_{14}B$ . *Phys. Rev. Lett.* **85**, 429–432 (2000).
47. Billington, D. et al. Unmasking the interior magnetic domain structure and evolution in Nd-Fe-B sintered magnets through high-field magnetic imaging of the fractured surface. *Phys. Rev. Mater.* **2**, 104413 (2018).
48. Kotani, Y. et al. Realization of a scanning soft X-ray microscope for magnetic imaging under high magnetic fields. *J. Synchrotron Radiat.* **25**, 1444–1449 (2018).
49. Perdew, J. P., Burke, K. & Ernzerhof, M. Generalized gradient approximation made simple. *Phys. Rev. Lett.* **77**, 3865–3868 (1996).
50. Ozaki, T. Variationally optimized atomic orbitals for large-scale electronic structures. *Phys. Rev. B* **67**, 155108 (2003).
51. Terasawa, A. & Gohda, Y. Hidden order in amorphous structures: extraction of nearest neighbor networks of amorphous Nd-Fe alloys with Gabriel graph analyses. *J. Chem. Phys.* **149**, 154502 (2018).
52. Hirosawa, S., Tokuhara, K. & Sagawa, M. Coercivity of surface grains of Nd-Fe-B sintered magnet. *Jpn J. Appl. Phys.* **26**, L1359 (1987).
53. Fischbacher, J. et al. Nonlinear conjugate gradient methods in micro-magnetics. *AIP Adv.* **7**, 045310 (2017).
54. Sepehri-Amin, H., Tang, X., Ohkubo, T. & Hono, K. Magnetization reversals of Nd-Fe-B-based magnets with different microstructural features. *JOM* **74**, 2328–2337 (2022).
55. Li, J. et al. On the temperature-dependent coercivities of anisotropic Nd-Fe-B magnet. *Acta Mater.* **199**, 288–296 (2020).
56. Koyama, T., Tsukada, Y. & Abe, T. Computational thermodynamics and microstructure simulations to understand the role of grain boundary phase in Nd-Fe-B hard magnets. *Sci. Technol. Adv. Mater.* **22**, 1–13 (2021).
57. Sepehri-Amin, H., Ohkubo, T., Shima, T. & Hono, K. Grain boundary and interface chemistry of an Nd-Fe-B-based sintered magnet. *Acta Mater.* **60**, 819–830 (2012).
58. Sasaki, T. T., Ohkubo, T. & Hono, K. Structure and chemical compositions of the grain boundary phase in Nd-Fe-B sintered magnets. *Acta Mater.* **115**, 269–277 (2016).
59. Soderžnik, M. et al. Magnetization reversal of exchange-coupled and exchange-decoupled Nd-Fe-B magnets observed by magneto-optical Kerr effect microscopy. *Acta Mater.* **135**, 68–76 (2017).
60. Murakami, Y. et al. Magnetism of ultrathin intergranular boundary regions in Nd-Fe-B permanent magnets. *Acta Mater.* **71**, 370–379 (2014).